sustainability

Article

Research on the Pounding Response and Pounding Effect of a Continuous Rigid-Frame Bridge with Fabricated Super-High Piers Connected by Grouting Sleeves

Shaojian Wang [1,†], Weibing Xu [1], Xiaomin Huang [2,†], Xiaoyu Yan [3], Jun Ma [4,*], Hang Sun [4], Jin Wang [5] and Yanjiang Chen [1]

1 Beijing Key Laboratory of Earthquake Engineering and Structural Retrofit, Beijing University of Technology, Beijing 100124, China
2 School of Architectural Engineering, Kunming University of Science and Technology, Kunming 650031, China
3 School of Engineering, Open University of China, Beijing 730030, China
4 School of Transportation Science and Engineering, Harbin Institute of Technology, Harbin 150006, China
5 School of Water Resources and Hydropower Engineering, North China Electric Power University, Beijing 100190, China
* Correspondence: majunlxd@163.com; Tel.: +86-13936319257
† These authors contributed equally to this work.

Abstract: The dynamic characteristics of a continuous rigid-frame bridge with fabricated super-high piers (CRFB-FSP) connected by grouting sleeves and adjacent continuous beam bridges (AB) are significantly different, and they are prone to pounding under earthquake excitation. At present, the pounding response between the CRFB-FSP and AB is still unclear, and the impact of the pounding on the seismic performance of a CRFB-FSP is still in the exploratory stage. In this study, two 1/20 scaled models of a CRFB-FSP (MB) and a cast-in-place AB were designed and manufactured. Then, according to the research purpose and the output performance of the shaking table, three each of non-long-period (NLP) ground motions and near-fault pulse-type (NFPT) ground motions were selected as the inputs of the excitation shaking table test. The peak ground acceleration (PGA) changes from 0.5 g to 1.5 g. According to the similarity ratio (1/20), the initial gap between the MB and AB was taken as 7 mm (prototype design: 140 mm). Furthermore, the longitudinal pounding response between the CFRB-FSP and AB, as well as its influence on the seismic performance of the CFRB-FSP, was systematically investigated through a shaking table test and finite element analysis (FEA). The results showed that the pounding with the CRFB-FSP easily caused a persistent pounding, which may increase the damage risk of the pier. The peak pounding force under the NFPT ground motion was more significant than under the NLP ground motion, whereas the pounding number under the NFPT ground motion was smaller. The peak pounding force increased with the increase in the initial gap, pounding stiffness, span, and pier height. With and without pounding, the CRFB-FSP reflected higher-order mode participation (HMP) characteristics. After pounding, under the NFPT excitation, the HMP contribution increased significantly compared with that of the without pounding condition, while this effect under the NLP excitation was smaller. The peak displacement of the main beam of the CRFB-FSP increased with the increase in the main beam span, pier height and initial gap. The peak bending moment of the pier bottom increased with the increase in the main beam span and initial gap, however, decreased with the increase in the pier height. Moreover, the peak displacement of the main beam and the peak moment of the pier bottom of the CRFB-FSP both reduced. In contrast, the corresponding seismic response of the AB increased under the same conditions.

Keywords: continuous rigid-frame bridge with fabricated super-high piers connected by grouting sleeves; higher-order mode; shaking table test; OpenSees; pounding

Citation: Wang, S.; Xu, W.; Huang, X.; Yan, X.; Ma, J.; Sun, H.; Wang, J.; Chen, Y. Research on the Pounding Response and Pounding Effect of a Continuous Rigid-Frame Bridge with Fabricated Super-High Piers Connected by Grouting Sleeves. *Sustainability* **2022**, *14*, 11334. https://doi.org/10.3390/su141811334

Academic Editors: Chengqing Liu, Zhiguo Sun and Ying Ma

Received: 20 July 2022
Accepted: 6 September 2022
Published: 9 September 2022

1. Introduction

A continuous rigid-frame bridge with super-high piers (CRFB-SP) has a superior space spanning ability and is very competitive with other bridge types in mountainous areas [1]. However, the environment and ecology are relatively fragile in mountainous areas. Therefore, the environmental and ecological protection has become a prominent problem in the current construction of cast-in-place bridges [2]. Moreover, a long cast-in-place construction period will significantly increase the possibility of CRFB-SP being subjected to accidental events, such as earthquakes, strong wind, and mudslides, since the whole system of CRFB-SP is not formed during the construction process. The resistant capacity of the CRFB-SP is relatively poor subjected to accidental events during the construction periods, especially in the cantilever stage [3]. The continuous rigid-frame bridge with fabricated super-high piers (CRFB-FSP) has the advantages of being cost effective, green, low-carbon, and environmentally friendly [4]. It is a development trend to construct CRFB-FSP replacing CRFB with cast-in-place super-high piers. However, CRFB-FSP is generally adjacent to a simply supported beam bridge or a continuous beam bridge in mountainous areas. Since the dynamic characteristics of the CRFB-FSP (MB) and AB are significantly different, they are prone to pound under the action of an earthquake [5,6].

In view of the significant impact of the pounding on the local damage and seismic performance of adjacent structures, scholars have carried out a series of studies on the pounding response and pounding effect on adjacent structures. For numerical analysis, Chen et al. [7], conducted a nonlinear time-history analysis of the pounding response between the inclined bridge and the abutment. The results showed that the longitudinal displacement and rotation angle increased with the increase in the skew angle. Zheng et al. [8], explored the pounding response law of curved bridges under near-fault ground motions based on an OpenSees platform. The results showed that the shear force of the bridge piers increased after considering the pounding. Zhao et al. [9], explored the impact of spatial ground motion on the pounding response of fabricated bridges by establishing a numerical model of the whole bridge with low fabricated piers. The results showed that compared to cast-in-place piers, the ground motion considering the spatial variation may cause more serious pounding damage to fabricated piers. Additionally, they [10] compared the pounding response laws of adjacent structures with different frequency ratios through numerical simulation analysis. The results showed that the maximum displacement response was generated when the frequency ratio was 1; the maximum pounding force was generated when the frequency ratio was 1.414. Shen et al. [11], studied the transverse pounding response of suspension bridges through numerical simulation. The results showed that under large-intensity earthquakes, the pounding between the beam and tower legs would significantly increase the seismic demands of the tower legs. Guo et al. [12], established a finite element model of a typical hybrid truss-girder bridge and studied the impact of the wave passage effect on pounding. The results showed that for this type of long-span girder bridge, even if the vibration period of adjacent bridges is similar, pounding may occur due to the influence of the wave passage effect. In addition, Wang, Jiao, and Leila et al. [13–15], also studied the pounding response of adjacent structures through numerical simulation. In view of the serious impact of pounding on the seismic performance of bridges, Jia and Zhou et al. [16,17], suggested using dampers or adjusting the bearing parameters to avoid the pounding.

Compared with the numerical analysis, the experimental study of the seismic performance of bridges considering pounding is more complicated. The existing experimental studies on the pounding response and influence of an entire bridge were almost entirely on cast-in-place bridges. Saidi et al. [18], used a continuous bridge to study the influence of the main girder-abutment interaction. The results showed that the pounding between the main girder and the abutment resulted in a large in-plane rotation of the main girder and significant residual displacement of the piers. Kun [19] studied the response of pounding between a straight bridge, two skewed bridges (skew angle: 30°/45°), and the abutments through shaking table tests. The results showed that for the straight bridges and 30° skewed bridges, the pounding with the abutment reduced the longitudinal relative displacement of the main beam; for 45° skewed bridges, the pounding increased the longitudinal relative displacement of the main beam. Bo et al. [20], used an artificial plastic hinge to simulate the plastic deformation of a pier and studied the inelastic pounding response of adjacent structures through the shaking table test. The results showed that the rotation number of the plastic hinge may increase under a pounding condition. Li et al. [21], explored the pounding response law of a 1/10 scale curved bridge model with longitudinal slope through shaking table tests. The results showed that the peak pounding force increased with the increase in the initial gap. Yang et al. [22], studied the seismic response of bridges with rocking footings through the shaking table test. The results showed that this type of bridge may generate a larger maximum bending moment than the fixed-base bridge under pounding conditions. For prefabricated bridges, the seismic performance of fabricated bridge piers was widely investigated [23–26], and the recent findings preliminarily verified that the prefabricated piers also had good seismic performance, especially the prefabricated piers connected by grouting sleeves [27–29].

It can be seen from the existing literature that the current research results of the adjacent pounding response and impact are still concentrated on bridge structures with medium and low piers, and most of them are concentrated on cast-in-place bridges. The grouting sleeve connection can be introduced in the prefabricated super-high piers. However, the research on the adjacent pounding response and impact of fabricated bridges with fabricated super-high piers, especially connecting by grouting sleeves, is scarce.

In view of this, this paper designed and manufactured scaled models of a CRFB-FSP (MB) and a cast-in-place adjacent bridge (AB) with a similarity ratio of 1/20. Firstly, the seismic performance of CRFB-FSP was investigated through shaking table tests, particularly the higher-order mode participation characteristics of the CRFB-FSP. Furthermore, the OpenSees finite element software was used to establish the overall nonlinear finite element model (FEM), considering the pounding between the MB and AB, and was verified based on the results of the pounding tests. Then, the pounding response and pounding effect between the MB and AB were systematically analyzed, particularly the influence law of initial gap, pounding stiffness, span, pier height on the above pounding response and pounding effect.

2. Experimental Design

2.1. Bridge Model Design

The prototype bridge in this test was a continuous rigid-frame bridge with cast-in-place super-high piers and its approach bridge (cast-in-place two-span continuous-girder bridge) located in a high-intensity area. The span of the continuous rigid-frame bridge with cast-in-place super-high piers (MB) was 88 + 166 + 88 m; the main beam was a single-box single-room concrete section. The main beam adopted a quadratic curve change from the root section (beam height: 8 m) to the middle (end) section (beam height: 3.5 m). The beam width was 12 m. C55 concrete was used. The piers were a reinforced concrete hollow thin-walled pier with variable section (piers height: 100 m). C40 concrete was used. The beam-end bearings of the MB were unidirectional sliding bearings. The vertical and horizontal bearing capacities were 40×10^3 kN and 6×10^3 kN, respectively. The friction coefficient was 0.02. The main beam of the AB was the same as the end section of the MB. C55 concrete was used. The piers were double-column piers (piers height: 27 m and 28 m). C40 concrete was used. The beam-end bearings of the AB were similar to that of the MB. The vertical and horizontal bearing capacities were 15×10^3 kN and 2.25×10^3 kN, respectively. The middle of the AB was a fixed bearing. The vertical and horizontal bearing capacities were 30×10^3 kN and 4.5×10^3 kN, respectively. The structural dimensions of the prototype bridge are shown in Figure 1. The pier heights of the MB and AB are significantly different, shown in Figure 1, which may easily cause pounding between the CRFB-SP and the adjacent bridges under earthquake excitation.

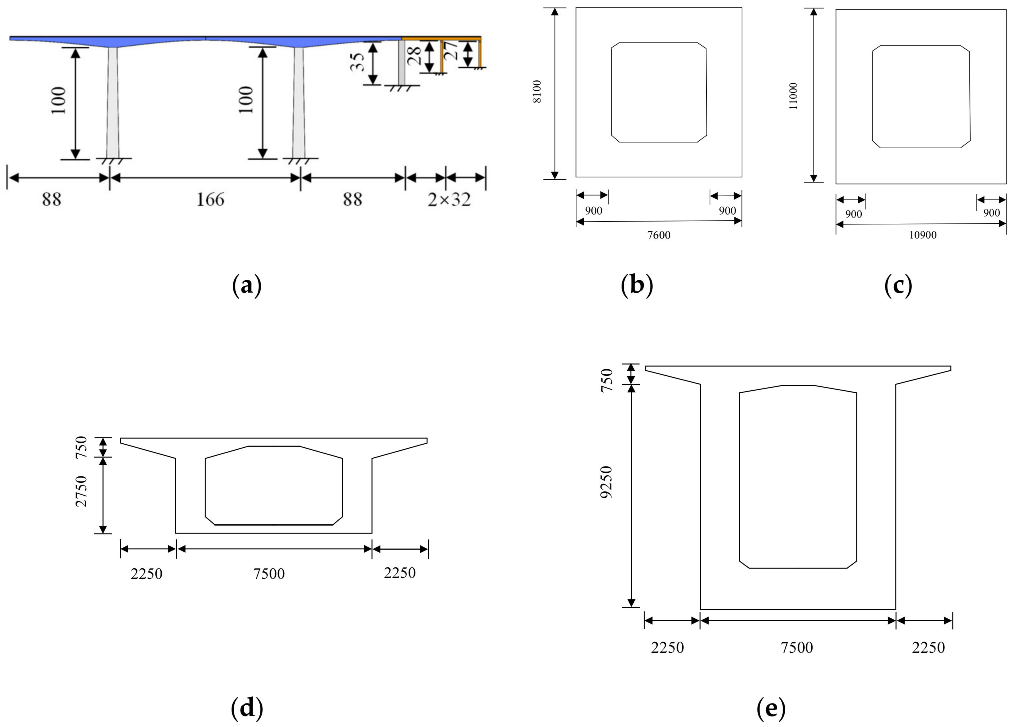

Figure 1. Structural dimensions of prototype bridge (mm). (**a**) Overall schematic of prototype bridge (m). (**b**) Pier top section (mm). (**c**) Pier bottom section (mm). (**d**) Section of main beam end (middle) (mm). (**e**) Section of main beam root (mm).

As mentioned in the introduction, grouting sleeve has the advantages of a simple structure, good connection performance and it is economical [27–29]. Accordingly, based on the design parameters of the prototype bridges, we designed a fabricated bridge model, also based on the research results of the seismic performance of fabricated concrete piers connected with grouting sleeves [25,30]. In practical application, the grouting sleeves prestressing combined connection method for super-high piers has been proposed by the authors, shown in Figure 2. The multi-configuration prefabricated pier wall and the cast-in-place bearing platform are connected by grouting sleeves; the vertical multi-configuration prefabricated pier wall segments are connected by grouting sleeves, while the horizontal ones are connected by local cast-in-place nodes and annular prestressed tendons. This kind of prefabricated super-high pier can effectively improve the effectiveness of segments connection and the integrity of fabricated components, and was selected as the prototype of the prefabricated model pier.

In this study, the geometric dimensions of the bridge model comprehensively consider the following factors, including the main research focus, the bearing capacity of the shaking table, the convenience of construction, as well as the economy. Accordingly, the bridge model adopted a hybrid design that satisfied the following conditions [31], which (1) can reflect the dynamic response law of the prototype bridge; (2) is applicable to the shaking table; (3) is convenient for design and construction; (4) is economical.

The bearing capacity of the shaking table is 100 kN $\times$ 1.0 g. Based on the trial calculation of the design similarity coefficients, the geometric scale of the bridge model was determined to be 1/20. Subsequently, the other similarity coefficients of the bridge model were all determined and shown in Table 1.

In addition, the scholars have found that the pounding response between the MB and AB is mainly affected by the dynamic characteristic properties of the MB and AB [21]. Accordingly, to keep the test or simulation condition of pounding more coincident and representative, the similarity of the basic dynamic characteristics of the MB and AB was selected as the main design principle of the bridge model. In other words, the similarity of overall basic static stiffness of the CRFB-FSP and the AB (discussed in Section 4.3.1) is selected as design principle of the bridge model.

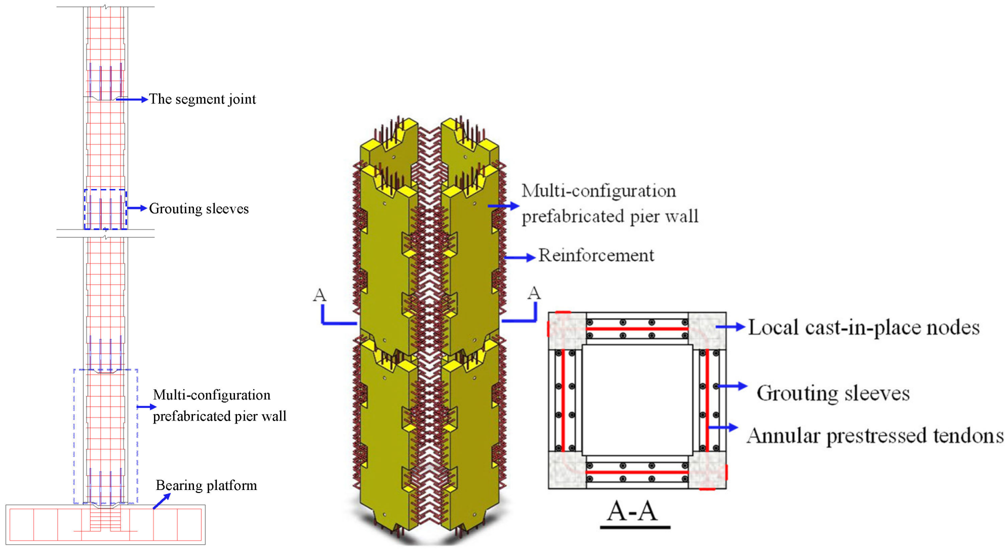

Figure 2. Design schematic of prefabricated super-high piers.

Table 1. Similarity coefficients of bridge models.

Physical Quantity	Dimension	Similarity Coefficient
Length	[L]	$S_L = 1/20$
Linear displacement	[L]	$S_\delta = S_L = 1/20$
Modulus of elasticity	$[ML^{-1}T^{-2}]$	$S_E = 1$
Density	[ρ]	$S_\rho = 1$
Equivalent mass density	$[\rho_0]$	$S_{\rho 0} = 4$
Force	$[MLT^{-2}]$	$S_F = 1/400$
Time	[T]	$S_T = 0.1$
Frequency	$[T^{-1}]$	$S_f = 1/S_t = 10$
Acceleration	$[LT^{-2}]$	$S_a = 5$
Quality	[M]	$S_m = S_F/S_a = 0.0005$

(1) CRFB-FSP models

According to the above experimental design principles, the prototype bridge (MB) was simplified into a "T"-shape. The total height of the "T"-shaped structure was 5.5 m, including 0.3 m for the main beam, 5 m for the pier, and 0.2 m for the bearing platform. The main beam was a linearly changing single-box single-room concrete section (root height: 300 mm; end height: 175 mm). The width was 600 mm. The pier was a hollow thin-walled section with a unified cross-section size (370 mm × 400 mm; wall thickness: 70 mm). The materials of each part of the bridge model were the same as that of the prototype bridge [32]. Along the height of the pier body, GT14 grouting sleeves (a total of five sleeve connection areas) were set at intervals of 1 m for the connection of pier segments. In order to artificially counterweight the piers, high-strength screw rods were evenly arranged along the height of the pier to fix the additional mass block. Due to the limitations of the laboratory conditions, the bearing platform was made of steel, with a section size of 720 mm × 720 mm × 200 mm. The reinforcement configuration information of the MB is listed in Table 2, and a schematic is shown in Figure 3a.

Table 2. Reinforcement information of bridge models.

Bridge Model	Component	Concrete	Longitudinal Reinforcement		Stirrup	
			Reinforcement	Reinforcement Ratio (%)	Standard Stirrup (Encrypted within 1.0 m from the Bearing Platform)	Stirrup Ratio (%)
Main bridge (MB)	Main beam	C55	6	3.1	Φ6@135	1.2
	Pier body	C40	14	2.1	Φ6@80 (Φ6@70)	1.9 (2.1)
Adjacent bridge (AB)	Main beam	C55	6	3.1	Φ6@135	1.2
	Pier body	C40	14	2.9	Φ6@80 (Φ6@70)	2.3 (2.5)

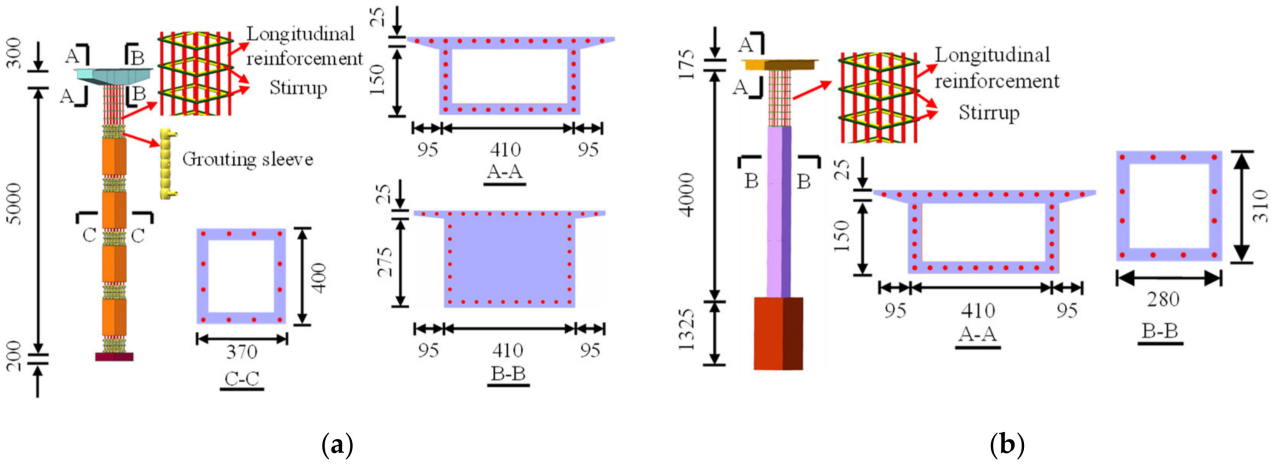

Figure 3. Dimensions of bridge model (mm). (**a**) CRFB- FSP. (**b**) AB.

(2) Adjacent bridge model

The design principles and methods of the AB bridge model were similar to those of the MB. The AB model was a cast-in-place "T"-shaped structure with a total height of 5.5 m (0.175 m for the main beam; 4 m for the pier; and 1.325 m for the bearing platform). The main beam was a single-box single-room concrete section (height: 175 mm; width: 600 mm). The pier was a hollow thin-walled section (section size: 280 mm × 310 mm; wall thickness: 47 mm). The reinforcement and concrete parameters of each component of the AB were the same as those of the MB. In order to manually counterweight the piers, the same setup as the MB bridge model was arranged. The bearing platform was similar to that of the MB, with a section size of 720 mm × 720 mm × 1325 mm. The reinforcement information is listed in Table 2, and a schematic is shown in Figure 3b.

2.2. Material Properties

To verify the material properties of each component, the mechanical properties of the materials used for the bridge model were tested on the shake table test date. The test results are shown in Table 3, according to which, the mechanical properties of all materials met the design requirements.

Table 3. Material characteristics.

Material Category	Grade	d (mm)	f_c, f_y (MPa)	f_t, f_u (MPa)	E (MPa)
Concrete	C40	/	46.7	2.6	34,300
	C55	/	55.1	3.8	34,400
Reinforcement	HRB400	6 (14)	455.1 (459.5)	589.3 (597.1)	208,000
	HPB300	6	418.3	580.2	206,000
Grouting sleeve	GT14	40	/	557.2	/

2.3. Layout of Measurement Points

To obtain the dynamic response of the key positions of the bridge model, strain sensors, laser displacement sensors, acceleration sensors, and wire-pull displacement gauges were arranged along the pier height. A force sensor was arranged at the end of the main beam of the MB (range: 20 t). The laser displacement measuring points of the CRFB-FSP MB were arranged every 1 m along the pier height in the direction of the ground motion excitation. The acceleration measuring points were arranged in the same way. The strain sensors were arranged on the bottom, middle, and top of the longitudinal bars, the middle of the pier bottom grouting sleeves, and the bottom and top areas of the concrete outer surfaces, respectively. The specific layout of the measuring points is shown in Figure 4. The shaking table test layout is shown in Figure 5. The main test sensors are shown in Figure 6.

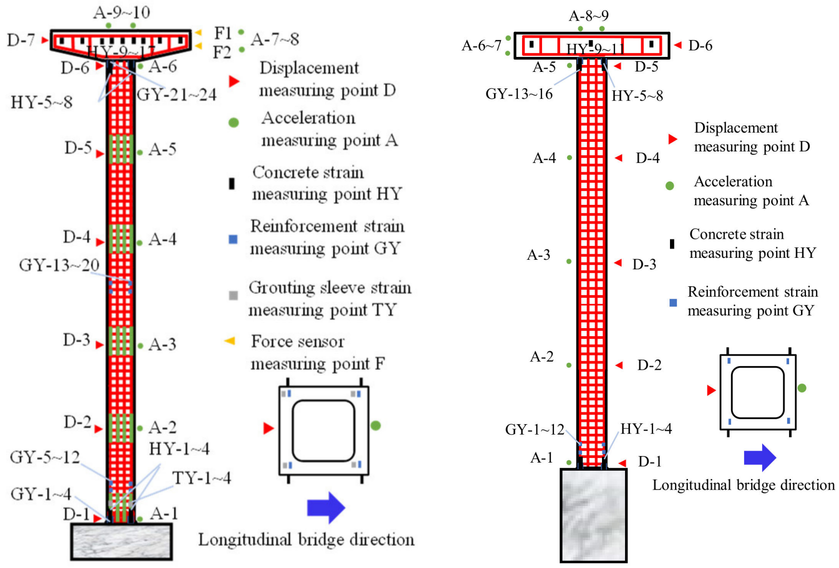

(**a**) (**b**)

Figure 4. Layout of measuring points of bridge model. (**a**) CRFB-FSP MB. (**b**) RC AB.

Figure 5. Shaking table test.

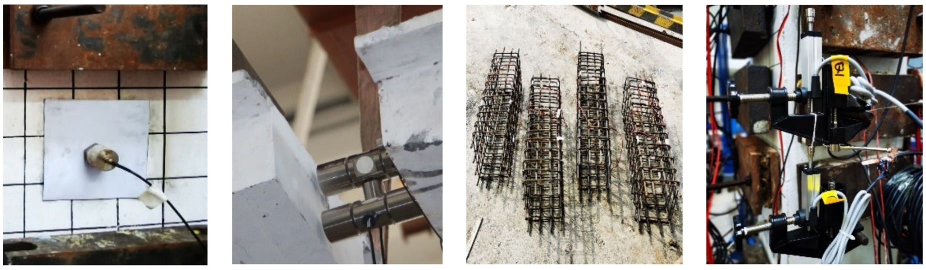

(**a**) (**b**) (**c**) (**d**)

Figure 6. Test sensor. (**a**) Acceleration sensors. (**b**) Force sensor. (**c**) Strain sensors. (**d**) Wire-pull displacement gauges.

2.4. Test Cases

Based on the seismic category of the prototype bridge (Class A) and the site type (Site B), the response spectrum was generated according to the Specifications for Seismic Design of Highway Bridges (JTG/T 2231-01-2020). The relevant ground motions were selected from the PEER database for the shaking table tests, including three each of the NLP and NFPT ground motions (NFPT$_{T_p \approx T_1}$, T_1 is the first-order mode period of the longitudinal bridge of the prototype bridge, referred to as NFPT). The selected ground motions were compressed according to the similarity theory as test seismic waves. The selected ground motions are shown in Table 4. The comparison between the selected ground motions and the design response spectrum is shown in Figure 7. As Figure 7 shows, near the first-order period (T_1 = 3.38 s) point of the prototype bridge, the selected NLP ground motion response spectrum value was basically consistent with the design response spectrum value. The mean square error was 5.5%. In the vicinity of the second-order and third-order periodic points, the mean square error was relatively large (27.5% and 15.1%, respectively). The NFPT response spectrum value near the characteristic period point was much larger than the design response spectrum value, which was related to its long period characteristic.

Table 4. Detailed parameters of ground motions.

Site Category	Ground Motion Type	Ground Motion	Fault Distance (km)	T_p (s)	PGA (g)
B	NLP	RSN503	56.7	-	0.037
		RSN40	129.1	-	0.041
		RSN55	111.3	-	0.012
	NFPT	RSN171	0.07	3.42	0.317
		RSN292	6.7	3.27	0.227
		RSN983	0.1	3.53	0.571

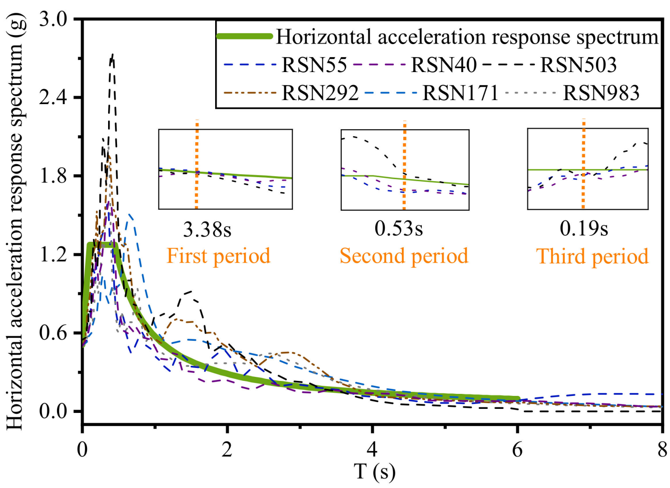

Figure 7. Comparison between the selected ground motions and the design response spectrum.

2.5. Test Condition Design

During the test, the ground motions were input along the longitudinal direction, according to the test conditions listed in Table 5. According to the similarity ratio, when the PGA input to the bridge model was 1.5 g, it was equivalent to a PGA input to the prototype bridge of 0.3 g. According to the design of the prototype bridge, the initial gap between the CRFB-FSP and AB was taken as 140 mm; according to the similarity ratio (1/20), it was 7 mm in the test.

Table 5. Shaking table test conditions.

Ground Motion Type	Ground Motion	PGA (g)
White noise	White noise	0.05
NLP	RSN503, RSN40, RSN55	0.5, 1.0, 1.5
NFPT	RSN292, RSN983, RSN171	
White noise	White noise	0.05

3. Test Results

3.1. Pounding Force

Figure 8 shows the time-history curve of the pounding force (*Pf*) between the CRFB-FSP and AB bridge models under typical ground motions with PGA = 1.5 g.

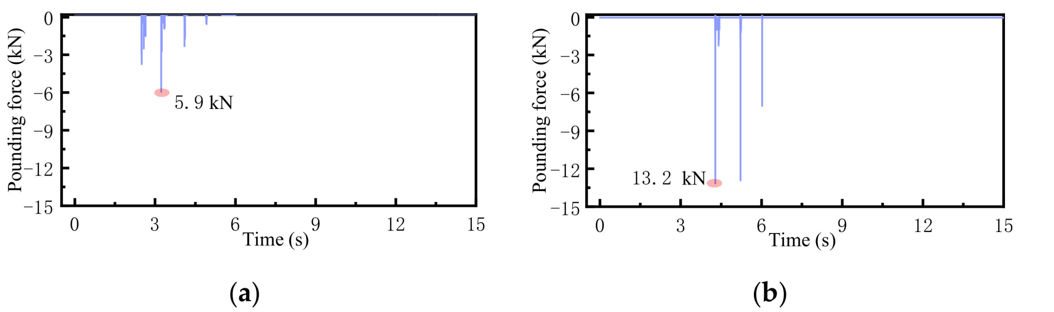

Figure 8. Time-history curve of the main beam pounding force. (**a**) RSN55 NLP. (**b**) RSN292 NFPT.

As Figure 8 shows, under the excitation of RSN55 and RSN292, the peak *Pfs* of CRFB-FSP were 5.9 kN and 13.2 kN; the pounding numbers were 4 and 3, respectively. The pounding may increase the damage risk and degree of the main beam and pier, which is consistent with the previous studies [14,21]. In addition, the pounding with the CRFB-FSP easily caused a persistent pounding, which may aggravate the damage of the bridge, especially for the seam joint at the pier bottom of the CRFB-FSP.

3.2. Displacement

Figures 9 and 10 show the displacement time-history curves of the CRFB-FSP model at 1/5 H, 4/5 H, and H (pier top, H = 5 m) from the pier bottom under typical ground motions.

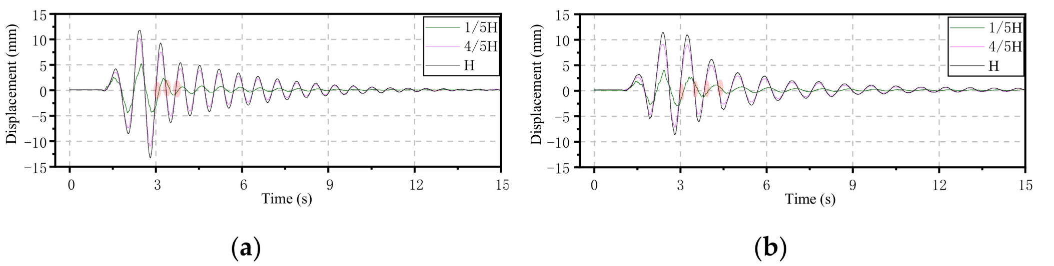

Figure 9. RSN55 (NLP) displacement time-history curve. (**a**) Without pounding PGA = 1.5 g. (**b**) With pounding PGA = 1.5 g.

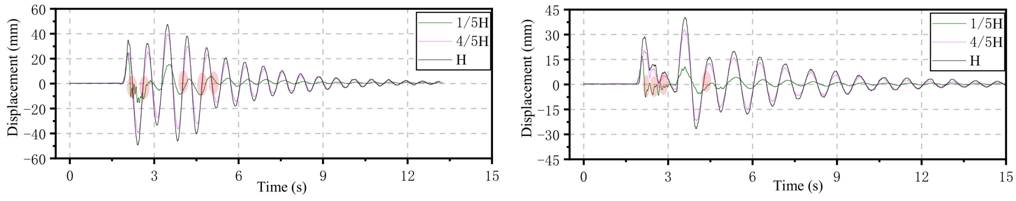

(**a**) (**b**)

Figure 10. RSN171 (NFPT) displacement time-history curve. (**a**) Without pounding PGA = 1.5 g. (**b**) With pounding PGA = 1.5 g.

As Figures 9 and 10 show, with and without pounding conditions, the displacements of the 1/5 H, 4/5 H, and H were in positive and negative directions of the baseline (displacement was 0) at the same time. This indicated that under the NLP and NFPT excitations, the higher-order mode contributed significantly to the displacement response of the super-high pier. The peak displacement of the pier top (main beam) under different ground motions was satisfied: $Ld_{\mathrm{NLP}} < Ld_{\mathrm{NFPT}}$, which is consistent with the results of Shen [33]. Previous studies indicated that the peak displacement was mainly dominated by the first-order mode [31]. However, from the above analysis, it can be observed that the HMP has an influence on the displacement in the off-peak displacement section. To further explore the effects of the higher-order mode, Table 6 shows the statistics of the characteristic time segments with HMP (time duration with HMP, which defined as the time duration that the displacements at typical pier heights were not on the same side of the center line of the pier), when the PGA = 1.5 g. The characteristic time segment was defined as the cumulative time of the displacement direction at 1/5 H being reversed to the displacement direction at 4/5 H and H.

Table 6. Statistics of the characteristic time segments of the CRFB-FSP model under various test conditions.

Ground Motion	PGA/g	Characteristic Time Segments CRFB-FSP	
		Without Pounding Cumulative Duration/s	With Pounding Cumulative Duration/s
NLP (RSN55)	1.5	0.38	0.51
NFPT (RSN171)		0.66	1.04

As Table 6 shows, with and without pounding conditions, the HMP under the NFPT excitation (without pounding: 0.66 s; with pounding: 1.04 s) was larger than that under the NLP excitation (without pounding: 0.38 s; with pounding: 0.51 s). When considering the pounding, under the NFPT excitation, the HMP contribution to the displacement increased significantly (+0.38 s, +57.6%), compared with the without pounding condition; meanwhile, this effect under the NLP excitation (+0.13 s, +34.2%) was smaller. This is because the NFPT ground motions often contain opposing and asymmetric velocity pulses [34]. When the NFPT positive pulse was input from the base, due to the large height of the super-high pier, the response of the pier top area lagged behind relative to the pier bottom area. This resulted in a significant phase difference in the displacement response.

Figure 11 shows the typical mode shapes of the bridge model with high-order modes significantly participating in the dynamic response, which were obtained by the Fourier cross correlation analysis of the dynamic response at different pier heights [21,31].

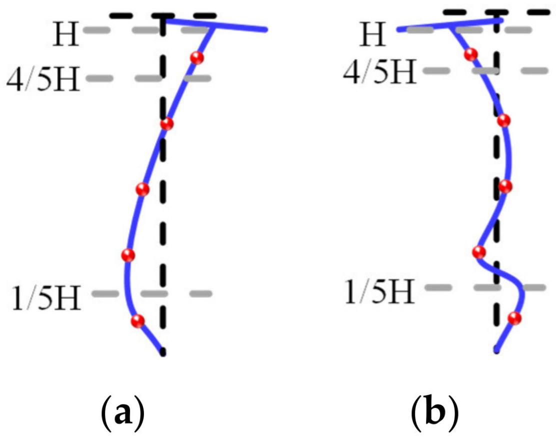

Figure 11. The mode shapes of the bridge model with high-order modes significant participation. (**a**) Under the RSN55 excitation with pounding. (**b**) Under the RSN171 excitation with pounding.

As shown in Figure 11, the high-order mode significantly participated in the dynamic response of the pier of the bridge model. That was, the displacements at 1/5H, 4/5H and H were on different sides of the baseline (center line of the pier).

3.3. Bending Moment Curvature

Figure 12 shows the M-φ curve of the pier bottom section of the CRFB-FSP model with and without pounding (the section of the upper edge of the grouting sleeves was selected as the pier bottom section for the CRFB-FSP).

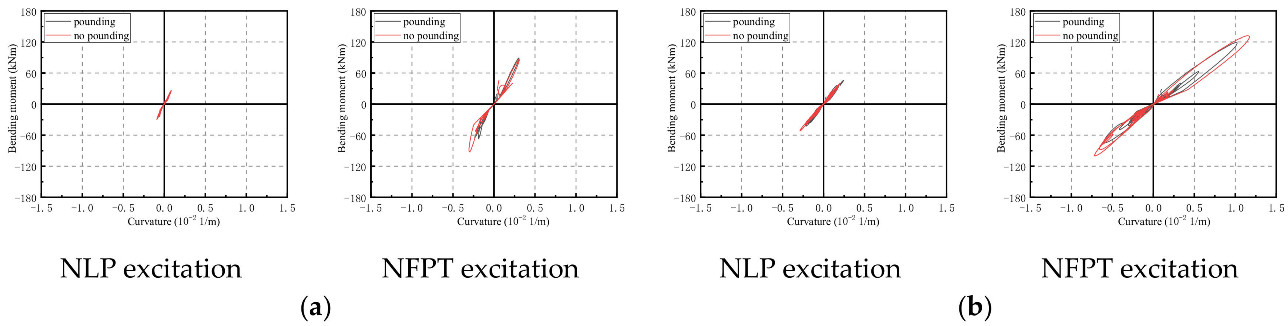

Figure 12. M-φ curve of pier bottom with and without pounding of the CRFB-FSP. (**a**) PGA = 1.0 g. (**b**) PGA = 1.5 g.

As Figure 12 shows, when PGA $\leq$ 1.0 g, the bridge model was in an elastic state, and the pier basically did not consume energy. When PGA = 1.5 g, the bridge model showed distinct elastic–plastic characteristics, and the pier began to consume energy. Considering the pounding, the bending moment of the pier bottom of the CRFB-FSP reduced, which was related to the pounding limiting the dynamic response of the MB to a certain extent. For example, under the NLP excitation, the peak bending moment of the pier bottom of the CRFB-FSP was reduced by 9.9% (no pounding: 53.4 kNm; pounding: 48.1 kNm), as similarly observed by Zheng [8]. Furthermore, the reduction rate under the NFPT excitation was relatively large compared to that under the NLP excitation. For example, under the NFPT excitation, the peak bending moment of the pier bottom of the CRFB-FSP was reduced by 16.5% (no pounding: 110.4 kNm; pounding: 92.2 kNm). This is because under the NFPT excitation, the pounding force between the MB and AB was relatively large. Accordingly, the constraint effect on the CRFB-FSP was more significant compared to that under the NLP excitation. On the other hand, the order of the peak bending moment of the pier bottom was satisfied: $M_{NLP} < M_{NFPT}$. This is because the long-period structures were sensitive to long-period ground motions. The NFPT ground motion was a long-period ground motion and carried a large amount of energy. The energy was input to the structure in a short time, resulting in a dynamic amplification effect [33,35].

4. Finite Element Analysis (FEA)

4.1. Finite Element Model (FEM)

To clarify the HMP characteristics of the CRFB-FSP, as well as the pounding response and pounding effect between the MB and AB, nonlinear finite element models (FEMs) of the prototype bridges need to be established. OpenSees has the advantages of efficient and practical algorithms, high modeling and calculation efficiency, and excellent programmability [36,37]. It is widely used in finite element analysis for seismic performance of structures [8–10], which is recommended by the Network for Earthquake Engineering Simulation (NEES) and the Pacific Earthquake Engineering Research Center (PEER). Accordingly, the nonlinear finite element models (FEMs) of the prototype bridges were established by OpenSees.

Since the main beam of a bridge generally maintains an elastic state, while the super-high piers are likely to be in an elastic–plastic state, the main beam of the CRFB-FSP was simulated by an Elastic Beam Column element with the elastic modulus of 3.55×10^4 MPa. The pier segments were simulated by a Force-Based Beam-Column element. The plastic hinges of the element were simulated by the Fiber Section. A Zero Length Section element [30] was used to simulate the segment joints. Steel02 was used to simulate the reinforcement.

As shown in Figure 13a, the Concrete01 model was used to simulate the cover and confined concrete of the segment joints without considering the tensile strength. For this model, the simulation concrete cannot bear any tensile load. On the contrary, the stress-strain of the compression part is based on the Kent-Park [38] model and consists of three parts: the parabola ascending section, the oblique straight line descending section, and the flat straight line residual section [36]. The Concrete01 model can effectively simulate the mechanical propertied of the segment joints. As shown in Figure 13b, the Concrete02 model assumes that the tensile elastic modulus of the concrete maintains constant before cracking. After cracking, a part of the simulation concrete between two adjacent cracks can still bear a certain tensile stress due to the bonding effect of the concrete. Therefore, the tensile stress-strain curve of the Concrete02 model adopts a linear ascending section and a linear descending section before and after the concrete cracking. Moreover, the Concrete01 and Concrete02 models are formed in basis of the concrete model of Kent-Park [38,39]. The compression stress-strain curve of the Concrete02 model is similar to that of the Concrete01 model. After reaching the compression peak point, the stress-strain curve of the Concrete02 model descends in the oblique straight line and then remains stable. Therefore, the Concrete02 model was used to simulate the cover and confined concrete of the pier segments considering the tensile strength. In summary, the Concrete01 model and Concrete02 model can effectively simulate the post-peak behavior of concrete with different mechanical properties, respectively. According to previous research [38,40], the mechanical properties of the concrete materials used for the bridge model are shown in Table 7.

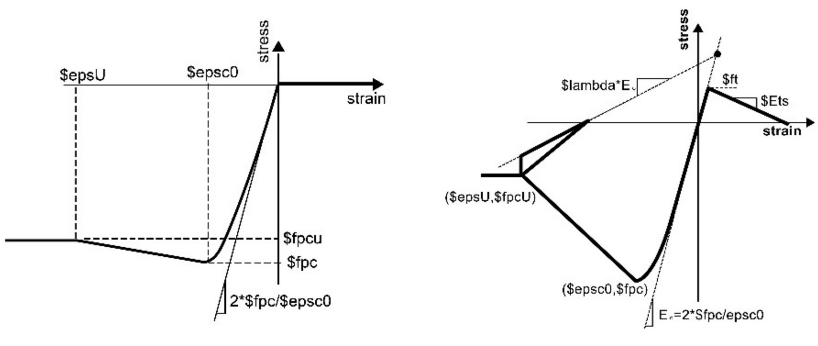

(**a**) (**b**)

Figure 13. Stress-strain relation for the concrete model. (**a**) Concrete01 model. (**b**) Concrete02 model.

Table 7. Concrete mechanical parameters of C40.

Concrete of C40		f_{pc}/MPa	epsc0	f_{pcu}/MPa	epscu	f_t/MPa	Ets/MPa
Concrete01	cover concrete	−21.2	−0.0020	−4.2	−0.0035	-	-
	confined concrete	−26.2	−0.0025	−5.2	−0.0190	-	-
Concrete02	cover concrete	−21.2	−0.0020	−4.2	−0.0035	2.4	1625
	confined concrete	−26.2	−0.0025	−5.2	−0.0190	2.6	1625

In this study, the grouting sleeves connection area was set every 5 m along the pier height. Elastic Uniaxial Material was used to simulate the grouting sleeves. The annular prestressing tendons was simulated by Truss element and Steel02 constitutive relationship. The main bridge pier–girder connection was simulated by a Rigid Link beam. The sliding bearings of the MB and the end of AB were simulated by a Zero Length element and Hysteretic nonlinear spring. The fixed bearing in the middle of the AB adopted similar elements and materials to the sliding bearing.

The simplified Hertz-Damp model was used to simulate the pounding, and the calculation of the relevant parameters of the model can be found in the literature [5,8]. The model parameters used in this study were calculated as follows: K_{t1} was 2.42×10^8 N/mm, K_{t2} was 5.44×10^7 N/mm, and δ_y was 2 mm. In addition, based on the research focus mentioned in the abstract, it was assumed that the pounding only occurs at the geometric center of the main beam. The FEM of the CRFB-FSP (MB) and the two-span continuous girder bridge (AB) are shown in Figure 14.

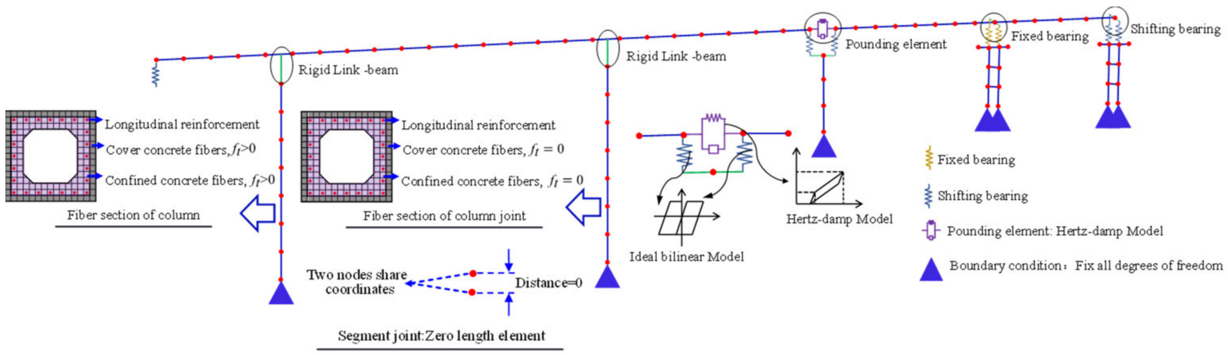

Figure 14. Schematic diagram of the FEM of the MB and AB considering pounding.

4.2. Test Condition and Test Cases

Three different spans were selected for the FEMs: 45 + 70 + 45 m (main span 70 m, mp-70), 72 + 120 + 72 m (main span 120 m, mp-120), and 88 + 166 + 88 m (main span 160 m, mp-160). To concentrate the analysis of variables, the AB parameters were consistent with the prototype AB. The initial gap between the CRFB-FSP and AB was taken as 140 mm. The test conditions are listed in Table 8.

Two ground motions were selected for each of the NLP and NFPT ($T_P \approx T_1$, the corresponding ground motions were selected according to the basic period of each MB in test conditions 1–12). The selection method was the same as that in Section 2.4. The PGA was chosen as 0.5 g, which was denoted as an E2 earthquake of 8-degree seismic fortification intensity.

Table 8. Structural parameter analysis condition table.

PGA/g	Parameter Type	Condition	Pier Height/m	Mp-/m	Initial Gap/mm	Pounding Stiffness
0.5	Pounding parameters	1	100	166	70	0.2 k
		2			140	0.5 k
		3			280	1.0 k
	Structural parameters	4	100	70	140	0.5 k
		5		120		
		6		166		
		7	130	70		
		8		120		
		9		166		
		10	160	70		
		11		120		
		12		166		

4.3. FEM Verification

4.3.1. Frequency

To verify the validity of the FEM and parameter selection, the CRFB-FSP (MB) and RC AB bridge model (scale ratio was 1/20), as well as the CRFB-FSP (MB) and RC AB prototype bridge (scale ratio was 1/1), were built using the method described in Section 4.1. Table 9 shows the experimental and FEA results of the initial frequency of the MB and AB.

Table 9. Initial frequency comparison between the experimental and FEA results of the MB and AB.

Bridge	Mode Order	Test Bridge Model (1/20) (Hz)	FEA (Hz)	
			Bridge Model (1/20)	Prototype Bridge (1/1)
CRFB-FSP MB (RC AB)	1	2.83 (4.05)	2.91 (4.25)	0.295 (0.423)
	2	18.68 (30.13)	19.05 (31.55)	1.901 (3.152)
	3	51.03 (57.80)	51.59 (59.93)	5.202 (5.997)

As shown in Table 9, the maximum frequency error rates between the FEA (MB + AB, 1/20; MB + AB, 1/1) and the experimental results were 4.7% (1/20) and 4.4% (1/1; this error was calculated by the similarity ratio of 10/1), respectively. The FEA results were in good agreement with the experimental results.

4.3.2. Displacement

In order to be similar to the shaking table test, the continuous ground motion was synthesized to obtain the dynamic response of the cumulatively damaged FEM. Each ground motion consisted of a combination of two identical ground motions and a 5 s zero-peak ground motion. The front and following ground motions were the same ground motion with different amplitudes (as shown in Figure 15). The front ground motion was input to the initial FEM to obtain the damaged FEM. Then, the following ground motion was input to obtain the dynamic response of the damaged FEM.

Figure 16 shows the displacement time-history curves of the CRFB-SFP main beam of the FEA (scale ratio was 1/20) and the test bridge model, under the pounding condition (RSN40 excitation; PGA = 1.5 g). As Figure 16 shows, they were in good agreement (test: 15.2 mm; FEA: 15.9 mm; error rate: 4.6%). For further comparison, Table 10 gives the experimental and FEA results of the mean peak displacement of the main beam under various test conditions. As shown in Table 10, the maximum error rate between the experimental and FEA (scale ratio was 1/20) results was 5.9%; the maximum error rate between the experimental and FEA (scale ratio was 1/1) results was 5.4% (calculated by the similarity ratio of 1/20). The FEA results were in good agreement with the experimental results.

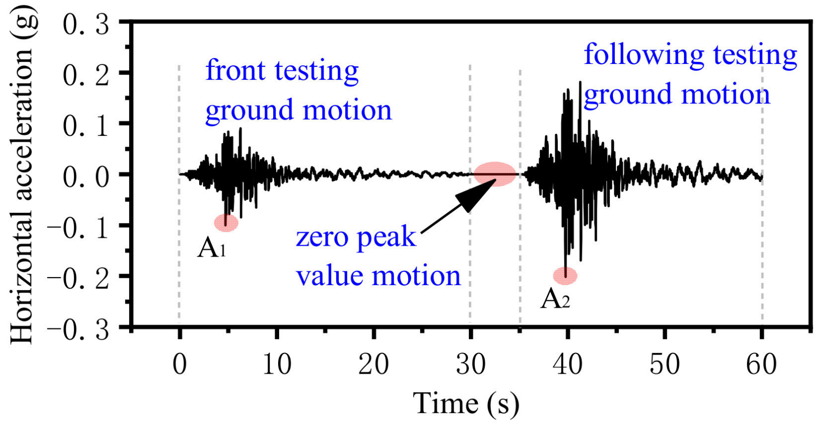

Figure 15. Combined ground motion. Note: A_1 was the PGA of the front testing ground motion; A_2 was the PGA of the following testing ground motion, and $A_2 = A_1 + 0.5$ g).

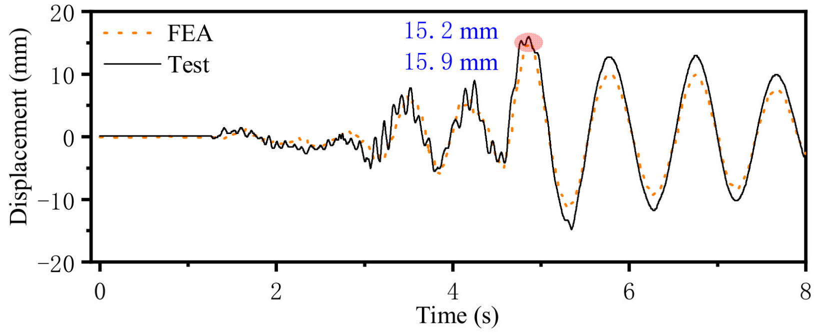

Figure 16. Displacement time-history curve of main beam.

Table 10. Comparison between the experimental and FEA results of the mean peak displacement of the main beam.

Ground Motion	PGA/g	Test Bridge Model (1/20)/mm	FEA/mm	
			Bridge Model (1/20)	Prototype Bridge (1/1)
NLP	0.5	5.3	5.5	114.0
	1.0	7.8	7.9	162.1
	1.5	13.5	13.2	278.1
NFPT	0.5	13.4	12.7	262.1
	1.0	21.8	20.5	422.2
	1.5	38.8	37.6	790.4

4.3.3. Pounding Force

Figure 17 shows the typical pounding force time-history curves of the CRFB-SFP main beam from the FEA (scale ratio was 1/20) and the test. As Figure 17 shows, the FEA results of the pounding number (test: 4; FEA: 4) and peak pounding force (test: 5.9 kN; FEA: 6.4 kN; error rate +8.5%) were in good agreement with the experimental results. The FEA also showed the persistent pounding characteristic. For further comparison, Table 11 gives the experimental and FEA results of the mean peak pounding force under various test conditions. As shown in Table 11, the maximum error rate between the experimental and FEA (scale ratio was 1/20) results was 9.8%; the maximum error rate between the experimental and FEA (scale ratio was 1/1) results was 9.4% (calculated by the similarity ratio of 1/400). The results met the analysis requirements. The large error rate of the pounding force may be related to the different pounding conditions between the experiment and the FEA.

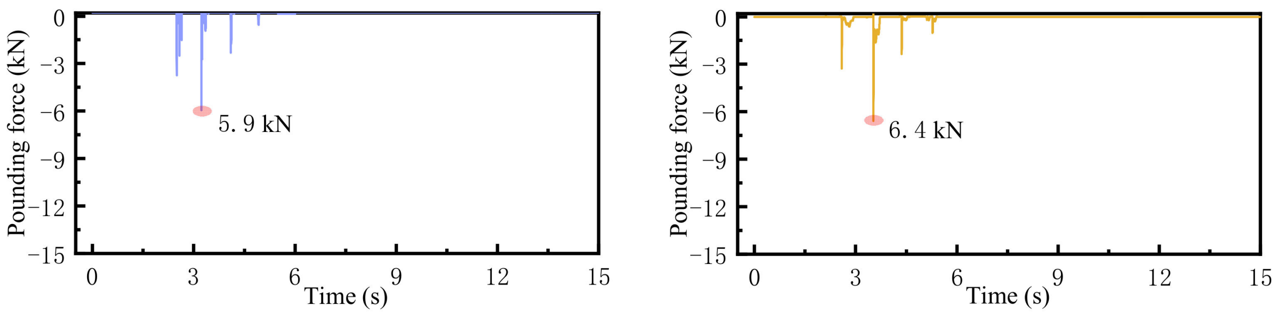

(**a**) (**b**)

Figure 17. Time-history curve of the main beam pounding force (under the RSN55 with the PGA = 1.5 g). (**a**) Test result. (**b**) FEA result.

Table 11. Comparison between the experimental and FEA results of the mean peak pounding force of the main beam.

Ground Motion	PGA/g	Test Bridge Model (1/20)/kN	FEA/kN	
			Bridge Model (1/20)	Prototype Bridge (1/1)
NLP	0.5	1.5	1.6	639.5
	1.0	2.7	2.5	1009.4
	1.5	5.7	6.0	2419.1
NFPT	0.5	2.9	2.7	1050.3
	1.0	4.8	5.1	2060.8
	1.5	11.2	12.3	4901.5

In summary, the FEA results were in good agreement with the experimental results. The FEMs can be used to study the pounding response and pounding effect between the CRFB-FSP and AB. To more intuitively reflect the dynamic response characteristics of the prototype bridge, the FEM of the prototype CRFB-FSP and prototype AB were used to conduct the FEA in the subsequent sections.

4.4. FEA Results

4.4.1. Initial Gap and Pounding Stiffness

(1) Pounding force

Figure 18 shows the variation in the mean peak pounding force of the CRFB-FSP main beam with the initial gap and pounding stiffness.

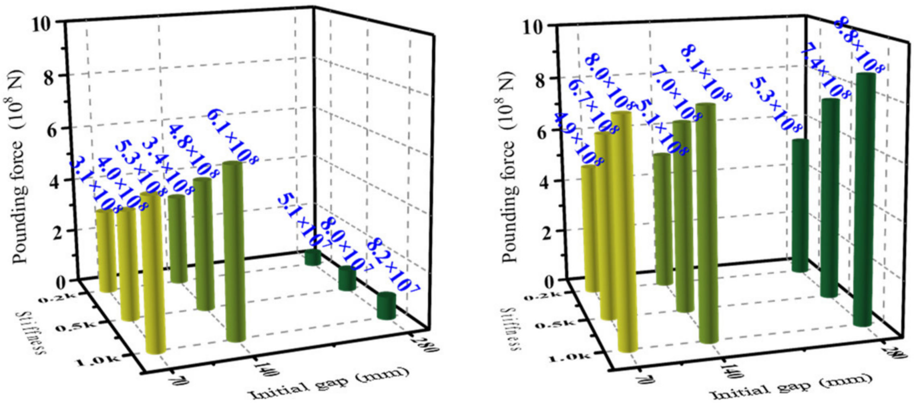

(**a**) (**b**)

Figure 18. Mean peak pounding force of the CRFB-FSP main beam. (**a**) under NLP excitation. (**b**) under NFPT excitation.

As Figure 18 shows, the peak pounding force of the main beam increased with the increase in the initial gap and pounding stiffness. For example, under the NFPT excitation with a pounding stiffness of 0.2 k, the peak pounding force with an initial gap of 140 mm and 280 mm increased by 4.1% and 8.2%, respectively, compared to that with an initial gap of 70 mm, as similarly observed by Li et al. [21]; under the NFPT excitation with an initial gap of 70 mm, the peak pounding force with a pounding stiffness of 0.5 k and 1 k increased by 36.7% and 63.3%, respectively, compared to that with a pounding stiffness of 0.2 k. However, the pounding may not occur when the initial gap was significant.

(2) Displacement

Figure 19 shows the variation in the mean peak displacement of the CRFB-FSP main beam with the initial gap and pounding stiffness (the displacement response law of pier top was close to the main beam).

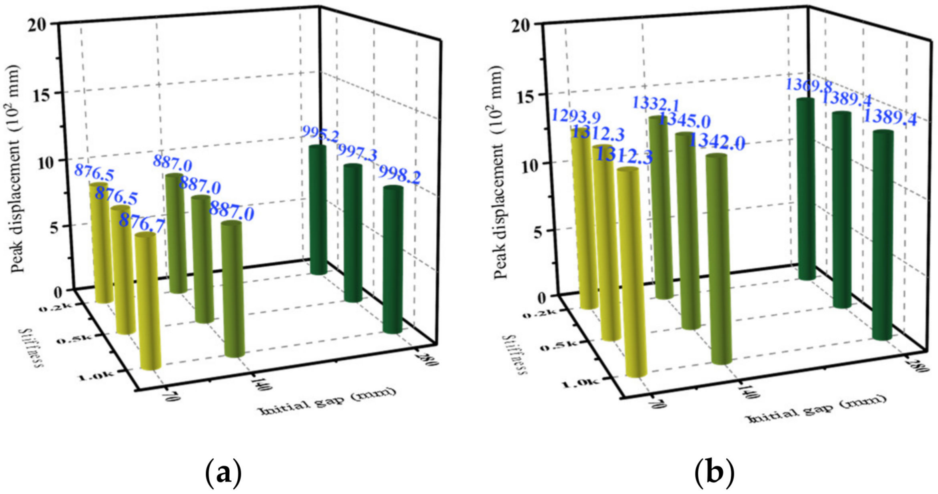

Figure 19. Mean peak displacement of the CRFB-FSP main beam. (**a**) under NLP excitation. (**b**) under NFPT excitation.

As Figure 19 shows, the peak displacement of the main beam increased slightly with the increase in the initial gap. For example, under the NFPT excitation with a pounding stiffness of 0.5 k, the peak displacement with an initial gap of 140 mm and 280 mm increased by 2.5% and 5.9%, respectively, compared to that with an initial gap of 70 mm. However, the peak displacement was not sensitive to the pounding stiffness, which is consistent with the previous research [10]. For example, under the NFPT excitation with an initial gap of 140 mm, the peak displacement with a pounding stiffness of 0.5 k and 1 k increased by 0.9% and 0.7%, respectively, compared to that with a pounding stiffness of 0.2 k.

(3) Bending moment

Figure 20 shows the variation in the mean peak bending moment of the pier bottom of the CRFB-FSP with the initial gap and pounding stiffness.

As Figure 20 shows, the peak bending moment of the pier bottom increased slightly with an increase in the initial gap. This is because the rotation of the pier increased as the gap increased, but the change in gap size from 70 mm to 280 mm was quite small compared to the bridge sizes, so the bending moment does not change significantly with the change in gap size. For example, under the NFPT excitation with a pounding stiffness of 0.2 k, the peak bending moment of the pier bottom with an initial gap of 140 mm and 280 mm increased by 2.0% and 3.0%, respectively, compared to that with an initial gap of 70 mm. However, the peak bending moment of the pier bottom was not sensitive to the pounding stiffness change, which is consistent with the previous research [10]. For example, under the NFPT excitation with an initial gap of 140 mm, the peak bending moment of the pier bottom with a pounding stiffness of 0.5 k and 1 k increased by 0% and 0.9%, respectively, compared to that with a pounding stiffness of 0.2 k.

It should be pointed out that the above results do not mean that a small gap of expansion joints or even no expansion joints can be set between practical adjacent bridges. A small gap size of expansion joints or even no expansion joints may obviously increase the secondary stresses of temperature change.

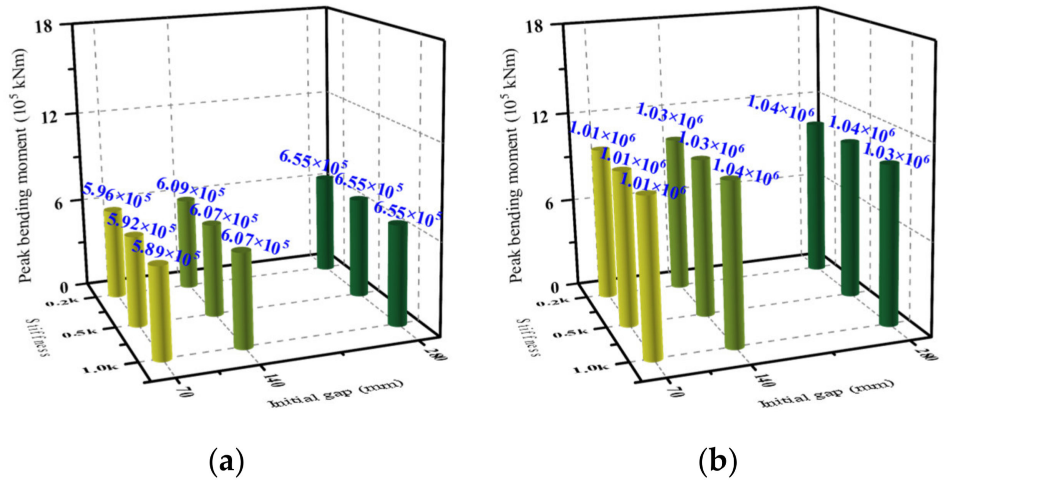

Figure 20. Mean peak bending moment of the pier bottom of the CRFB-FSP. (**a**) under NLP excitation. (**b**) under NFPT excitation.

4.4.2. Span and Pier Height

(1) Pounding force

Figure 21 shows the variation in the mean peak pounding force of the CRFB-FSP main beam with the changes in the span and pier height.

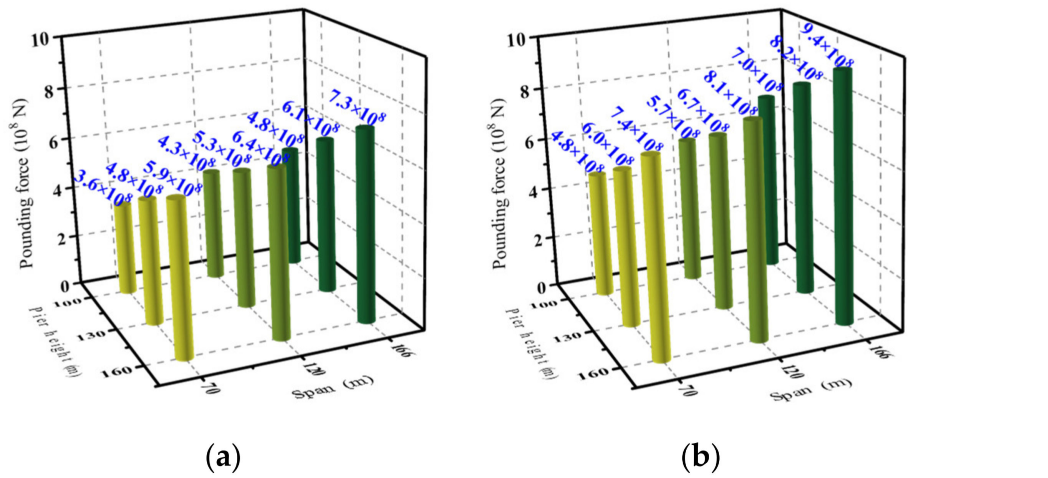

Figure 21. Mean peak pounding force of the CRFB-FSP main beam. (**a**) under NLP excitation. (**b**) under NFPT excitation.

As Figure 21 shows, the peak pounding force of the main beam increased with the increase in the span and pier height. For example, under the NLP excitation with a pier height of 100 m, the peak pounding force with a span of 120 m and 166 m increased by 19.4% and 33.3%, respectively, compared to that with a span of 70 m; under the NLP excitation with a span of 120 m, the peak pounding force with a pier height of 130 m and 160 m increased by 23.3% and 48.8%, respectively, compared to that with a pier height of 100 m. This is because the initial stiffness of the CRFB-FSP decreased as the span and pier height increased [33]. The difference in the displacement response between the CRFB-FSP and AB increased. Further, the "intrusion displacement" between the CRFB-FSP and AB increased, and the pounding force increased.

(2) Displacement

Figure 22 shows the variation in the mean peak displacement of the CRFB-FSP main beam with the changes in the span and pier height.

As Figure 22 shows, the peak displacement of the main beam increased with the increase in the span and pier height. For example, under the NFPT excitation with a pier height of 130 m, the peak displacement with a span of 120 m and 166 m increased by 16.2% and 33.9%, respectively, compared to that with a span of 70 m; under the NFPT excitation with a span of 120 m, the peak displacement with a pier height of 130 m and 160 m increased by 19.5% and 36.9%, respectively, compared to that with a pier height of 100 m. This is because the initial stiffness of the CRFB-FSP decreased with the increased span; meanwhile, the mass of the main beam increased. Accordingly, the displacement of the main beam increased. Moreover, the initial stiffness of the bridge decreased with the increased pier height, and the high-flexibility characteristic was more significant.

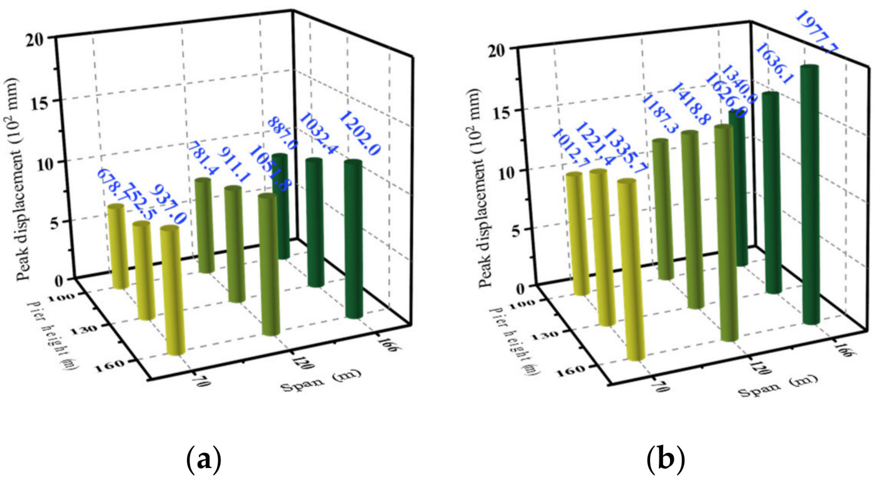

Figure 22. Mean peak displacement of the CRFB-FSP main beam. (**a**) under NLP excitation. (**b**) under NFPT excitation.

Figure 23 shows the typical displacement time history curve of the main beam of the CRFB-FSP. Figure 24 shows the typical variation in the mean peak displacement of the main beam of the CRFB-FSP with different pier heights and spans.

As shown in Figure 23, under the RSN55 excitation with a span of 120 m, the peak displacement with a pier height of 160 m increased by 31.0%, compared to that with a pier height of 100 m; under the RSN55 excitation with a pier height of 100 m, the peak displacement with a span of 166 m increased by 27.5%, compared to that with a span of 70 m. As Figure 24 shows, compared with the no pounding condition, the mean peak displacement of the main beam was reduced after considering the pounding. The reduction rate increased with the increase in the span and pier height. For example, under ground motion excitations with a pier height of 130 m, the reduction rate with a span of 166 m increased by 16.6% compared to that with a span of 70 m; under ground motion excitations with a span of 120 m, the reduction rate with a pier height of 160 m increased by 13.7% compared to that with a pier height of 100 m. Further, the reduction rate under the NFPT excitation was larger than that under the NLP excitation. This is because the pounding force increased with the increase in the span and pier height. In addition, the pounding force under the NFPT excitation was larger than that under the NLP excitation. The greater the pounding force, the more significant the constraint on the main beam of the CRFB-FSP. It should be noted that, after considering the pounding, the peak displacement of the main beam of the AB increased, because the pounding force had a restraining effect on the MB and a driving effect on the AB. As the span of the MB increased, the driving effect was more obvious. The growth rate of the displacement of the AB increased with the increase in the span and pier height of the MB. The growth rate under the NFPT excitation was larger than that under the NLP excitation.

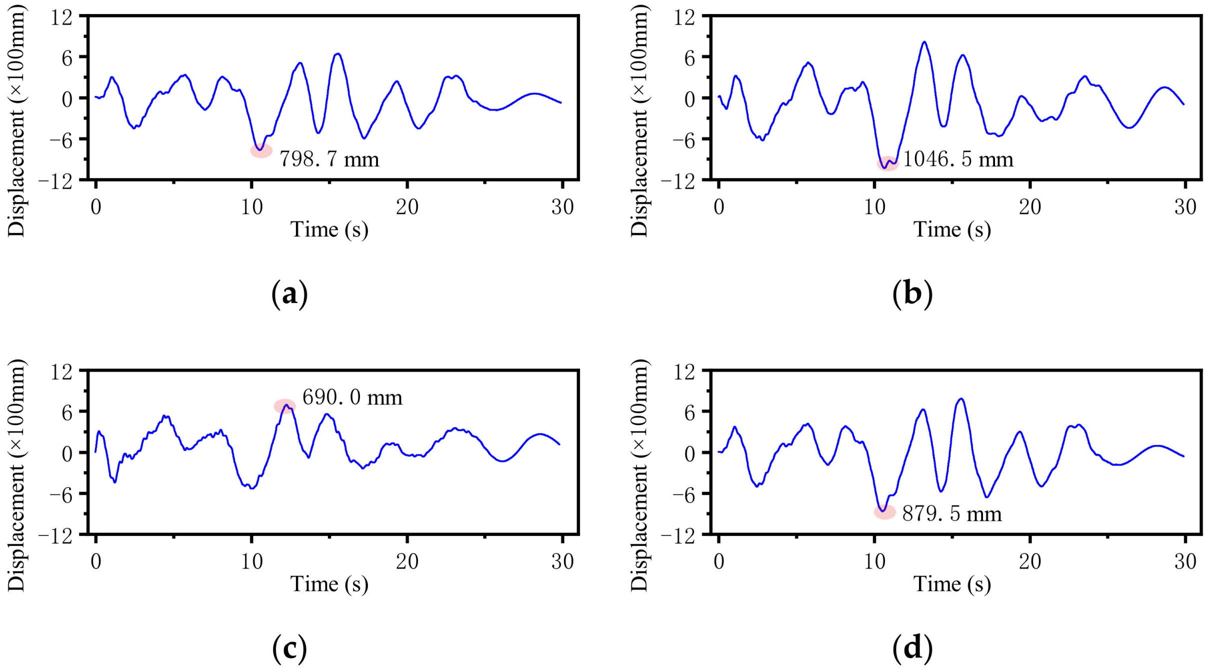

Figure 23. The displacement time history of the CRFB-FSP main beam under the NLP (RSN55) excitation. (**a**) Main span of 120 m with pier height of 100 m. (**b**) Main span of 120 m with pier height of 160 m. (**c**) Pier height of 100 m with main span of 70 m. (**d**) Pier height of 100 m with main span of 166 m.

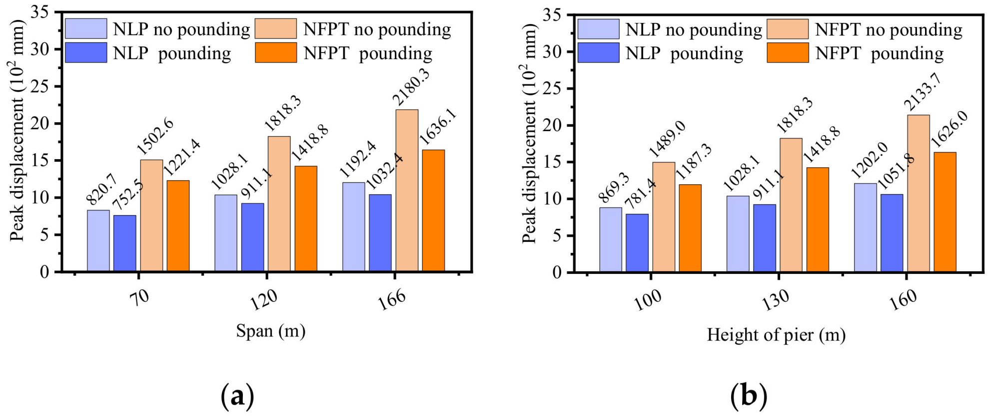

Figure 24. Peak displacement mean response of the main beam. (**a**) Pier height of 130 m. (**b**) Span of 120 m.

(3) Bending moment

Figure 25 shows the variation in the mean peak bending moment of the pier bottom of the CRFB-FSP with the changes in the span and pier height.

As Figure 25 shows, the peak bending moment of the pier bottom increased with the increase in the span. For example, under the NFPT excitation with a pier height of 130 m, the peak bending moment of the pier bottom with a span of 120 m and 166 m increased by 16.6% and 34.9%, respectively, compared to that with a span of 70 m. It should be noted that the recent findings on medium and low piers indicated that the peak bending moment of the pier bottom increased with the increase in the pier height [22]. However, from Figure 25, it can be observed that the peak bending moment of the pier bottom decreased with the increase in the pier height. For example, under the NFPT excitation with a span of 120 m, the peak bending moment of pier bottom with a pier height of 130 m and 160 m decreased by 8.6% and 16.8%, respectively, compared to that with a pier height of 100 m. This is because for bridges with middle and low piers, the bending moment of the pier bottom and the pier top displacement are closely related. They were mainly controlled by the first-order mode [31]. While, for bridges with for super-high piers, the bending moment of the pier bottom was jointly affected by the multi-order modes. With the increase in the pier height, the high-flexibility characteristics of the bridge and the HMP were more significant (especially when the structure entered the elastic–plastic stage). The bending moment direction of the pier bottom section (and the pier body section) caused by each mode was not the same, which led to a more complex variation law of the peak bending moment of the pier bottom section.

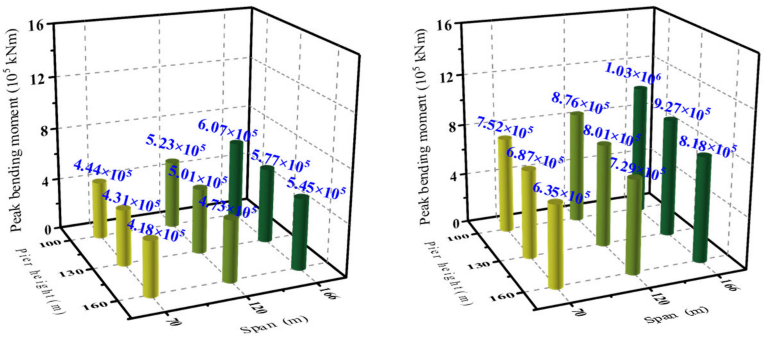

(**a**) (**b**)

Figure 25. Mean peak bending moment of the pier bottom of the CRFB-FSP. (**a**) under NLP excitation. (**b**) under NFPT excitation.

Figure 26 shows the typical bending moment time history curve of the pier bottom of the CRFB-FSP. Figures 27 and 28 show the typical M-φ curves with and without the pounding with a main beam span of 166 m.

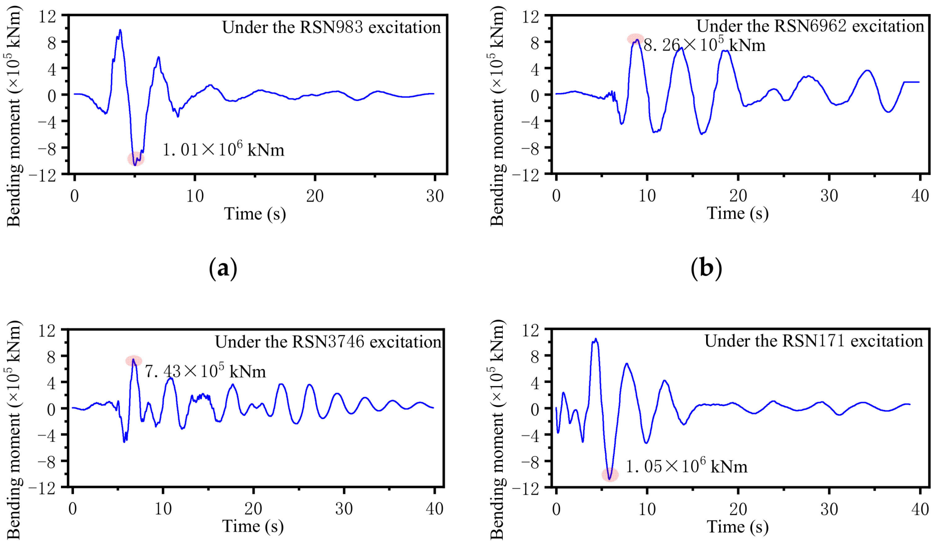

(**a**) (**b**)

(**c**) (**d**)

Figure 26. The bending moment time history of the pier bottom of the CRFB-FSP under NFPT excitations. (**a**) Main span of 166 m with pier height of 100 m. (**b**) Main span of 166 m with pier height of 160 m. (**c**) Pier height of 100 m with main span of 70 m. (**d**) Pier height of 100 m with main span of 166 m.

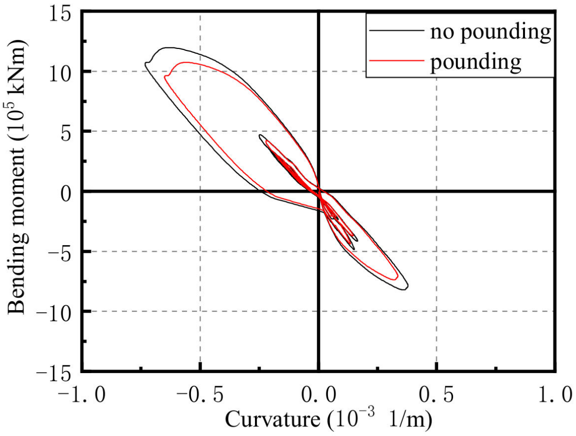

(**a**)

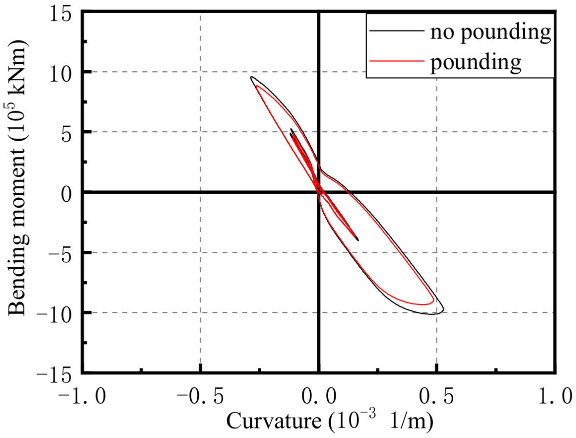

(**b**)

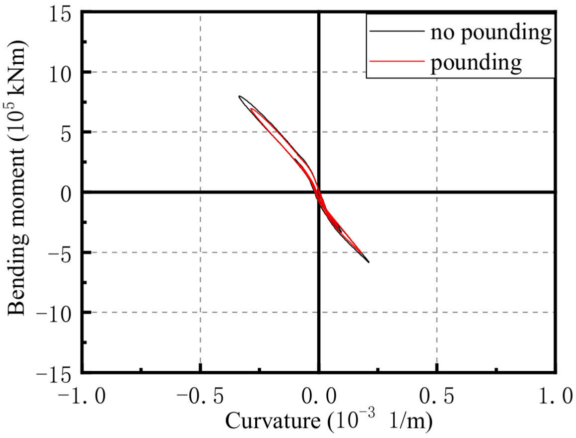

(**c**)

Figure 27. M-φ curve with a pier height of 100 m. (**a**) Pier bottom. (**b**) Pier middle. (**c**) Pier top.

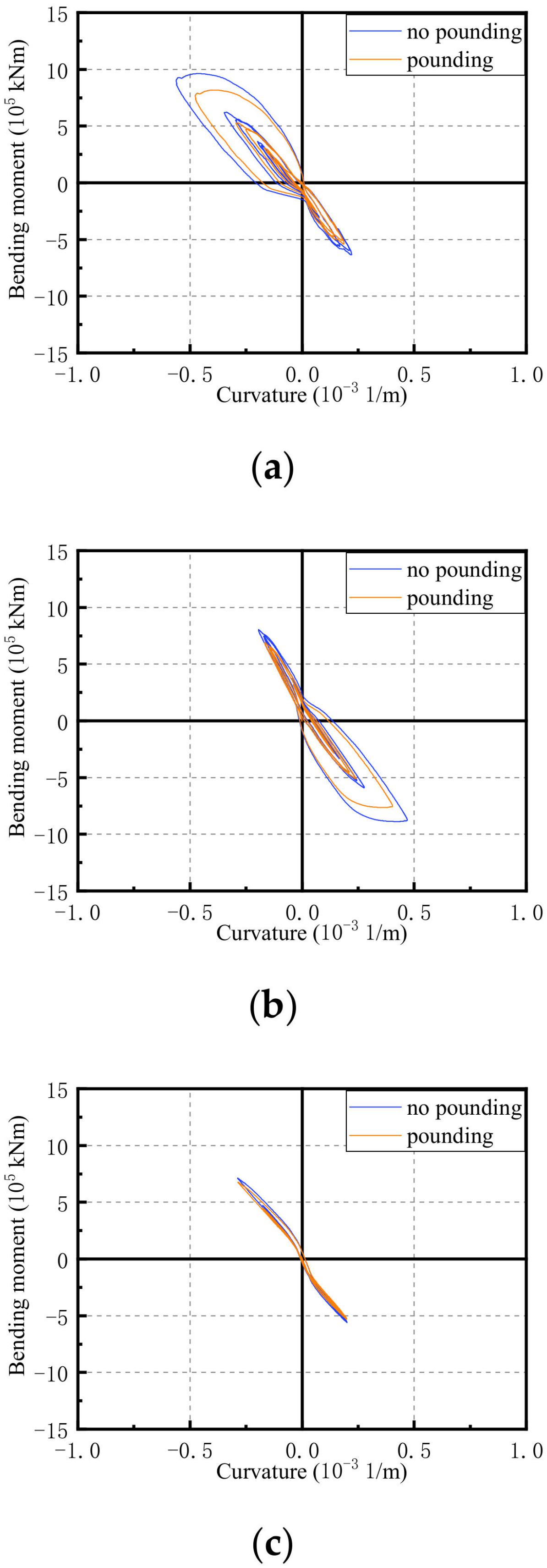

Figure 28. M-φ curve with a pier height of 160 m. (**a**) Pier bottom. (**b**) Pier middle. (**c**) Pier top.

As shown in Figure 26, under the NFPT excitation with a span of 166 m, the peak bending moment of pier bottom with a pier height of 160 m decreased by 18.2%, compared to that with a pier height of 100 m; under the NFPT excitation with a pier height of 100 m, the peak bending moment of the pier bottom with a span of 166 m increased by 41.3%, compared to that with a span of 70 m. As Figures 27 and 28 show, compared with the no pounding condition, the bending moment of the MB decreased after the pounding. The reduction rate increased with the increase in the span and pier height, and the reduction rate under the NFPT excitation was greater than that under the NLP excitation. For example, when the pier height was 100 m and 160 m, the bending moment of the pier bottom decreased by 12.9% and 17.5%, respectively. The reasons were similar to those described in Section 4.4.2. In addition, compared with the no pounding condition, the pier bottom bending moment of the AB increased after the pounding. The growth rate increased with the increase in the span and pier height of the MB (maximum growth rate: +18.2%), and the growth rate under the NFPT excitation was greater than that under the NLP excitation.

In summary, in the seismic design of super-high piers, attention should be paid to the bending moment demands of super-high piers which may increase with the decrease in the pier height. In addition, the pounding will reduce the peak displacement of the main beam and the peak bending moment of the pier bottom of the CRFB-FSP (MB). However, the corresponding seismic response of the AB increased under the same conditions, which should not be ignored in engineering practice. Moreover, the influence of spatial variation in ground motions on the pounding response and effect of CRFB-FSP, the seismic performance of CRFB-FSP with other types of fabricated connections (e.g., socket connection, hybrid connection), as well as the establishment of seismic design methods for CRFB-FSP need to be addressed in future studies.

5. Conclusions

In this study, the longitudinal pounding response between the CRFB-FSP and AB, its influence on the seismic performance of the CRFB-FSP and AB, as well as the higher-order mode participation (HMP) characteristics of the CRFB-FSP were systematically investigated through the shaking table test and finite element analysis (FEA). The following conclusions were drawn.

1. The peak pounding force under different ground motions was satisfied: $Pf_{\mathrm{NLP}} < Pf_{\mathrm{NFPT}}$. However, the pounding number under the NFPT excitation was relatively small. The peak pounding force increased with the increase in the initial gap, pounding stiffness, span, and pier height. In addition, the CRFB-FSP was prone to persistent pounding, which may increase the damage risk of the prefabricated super-high pier.
2. With and without poundings, the CRFB-FSP reflected higher-order mode participation (HMP) characteristics, and the HMP under the NFPT excitation was larger than that under the NLP excitation. When considering the pounding, under the NFPT excitation, the HMP contribution increased significantly compared with that of the without pounding condition, while this effect under the NLP excitation was smaller. When the high-order mode significantly participates the dynamic response of the pier, the displacements at different pier heights will be on different sides of the center line of the pier.
3. The peak displacement of the pier top and peak bending moment of the pier bottom of the CRFB-FSP slightly increased with the increase in the initial gap. However, the pounding stiffness had no obvious effect on them. The peak displacement of the main beam (pier top) of the CRFB-FSP increased with the increase in the main beam span and pier height. The peak bending moment of the pier bottom increased with the increase in the main beam span but decreased with the increase in the pier height. After pounding, the peak displacement of the pier top and the peak bending moment of the pier bottom of the CRFB-FSP were reduced, especially when the span and pier height increased and under the NFPT ground motions. In contrast, the corresponding seismic response of the AB increased under the same conditions.

Author Contributions: Conceptualization, W.X. and J.M.; methodology, S.W. and W.X.; software, S.W.; validation, X.H., X.Y., H.S. and J.W.; data curation, S.W.; writing—original draft preparation, S.W.; writing—review and editing, S.W., W.X. and J.M.; supervision, Y.C.; funding acquisition, W.X. and Y.C. All authors have read and agreed to the published version of the manuscript.

Funding: This study was partly supported by the National Natural Science Foundation of China (Grant No. 52108428, 52178446, 51978021, 51908015).

Institutional Review Board Statement: Not applicable.

Informed Consent Statement: Not applicable.

Data Availability Statement: All data generated or analyzed during this study are included in this article.

Conflicts of Interest: The authors declare that they have no known competing financial interest or personal relationships that could have influenced the work reported in this paper.

Nomenclature

CRFB-SP	continuous rigid-frame bridge with super-high piers
CRFB-FSP	continuous rigid-frame bridge with fabricated super-high piers
AB	adjacent continuous beam bridge (approach bridge)
MB	main bridge
NLP	non-long-period
NFPT	near-fault pulse-type
FEA	finite element analysis
FEM	finite element model
PGA	peak ground acceleration
HMP	higher-order mode participation
GT	grouting sleeve
PEER	Pacific Earthquake Engineering Research Center
Pf	pounding force
Ld	longitudinal displacement
Mp	main span

References

1. Huang, J.; Tan, P.; Zhang, Y.; Zhou, F. Endurance time analysis of seismic performances of long-span continuous rigid-frame bridges with corrugated steel webs. *Structures* **2022**, *43*, 990–1001. [CrossRef]
2. Li, X.; Li, L. Research on Green Evaluation of Mountainous Highway Construction. In *International Symposium on Advancement of Construction Management and Real Estate*; Springer: Singapore, 2020; pp. 727–745. [CrossRef]
3. Dong, X.M. Instability Analysis of High Pier of Continuous Rigid Frame Bridges. *Appl. Mech. Mater.* **2012**, *178*, 1989–1993. [CrossRef]
4. Tavares, V.; Gregory, J.; Kirchain, R.; Freire, F. What is the potential for prefabricated buildings to decrease costs and contribute to meeting EU environmental targets? *Build. Environ.* **2021**, *206*, 108382. [CrossRef]
5. Miari, M.; Choong, K.K.; Jankowski, R. Seismic Pounding Between Bridge Segments: A State-of-the-Art Review. *Arch. Comput. Methods Eng.* **2020**, *28*, 495–504. [CrossRef]
6. Shrestha, B.; Hao, H.; Bi, K. Devices for protecting bridge superstructure from pounding and unseating damages: An overview. *Struct. Infrastruct. Eng.* **2017**, *13*, 313–330. [CrossRef]
7. Chen, J.; Han, Q.; Liang, X.; Du, X. Effect of pounding on nonlinear seismic response of skewed highway bridges. *Soil Dyn. Earthq. Eng.* **2017**, *103*, 151–165. [CrossRef]
8. Zheng, Y.; Wang, J.; Xu, W.; Li, N.; Zhang, W.; Chen, Y. Impact of Near-Fault Ground Motions on Longitudinal Seismic Response of CHRF Bridges. *Sustainability* **2022**, *14*, 3591. [CrossRef]
9. Zhao, L.; Hao, H.; Bi, K.; Li, X. Numerical study of the seismic responses of precast segmental column bridge under spatially varying ground motions. *J. Bridge Eng.* **2018**, *23*, 04018096. [CrossRef]
10. Zhao, L.; Bi, K.; Hao, H.; Li, X. Numerical studies on the seismic responses of bridge structures with precast segmental columns. *Eng. Struct.* **2017**, *151*, 568–583. [CrossRef]
11. Shen, Y.; Li, J.; Freddi, F.; Igarashi, A.; Zhou, J. Numerical investigation of transverse steel damper TSD seismic system for suspension bridges considering pounding between girder and towers. *Soil Dyn. Earthq. Eng.* **2022**, *155*, 107203. [CrossRef]
12. Guo, W.; Li, J.; Guan, Z.; Chen, X. Pounding performance between a seismic-isolated long-span girder bridge and its approaches. *Eng. Struct.* **2022**, *262*, 114397. [CrossRef]

13. Wang, H.; Zhao, K.; Qin, S. Seismic Performance Assessment of a Pin-bearing Restraint System for Curved Bridge. *Period. Polytech. Civ. Eng.* **2022**, 1–10. [CrossRef]
14. Jiao, C.; Lu, J.; Wang, C.; Long, P.; Sun, Z. Experimental and numerical investigations on the effects of radius of curvature and longitudinal slope on the responses of curved bridges subject to seismic pounding. *Meas. Control* **2021**, *54*, 519–537. [CrossRef]
15. Khakzand, L.; Jalali, R.S.; Veisi, M. Near-fault ground motion effects on pounding and unseating using an example of a three-span, simply supported bridge. *Earthq. Eng. Resil.* **2022**, *1*, 164–195. [CrossRef]
16. Jia, H.Y.; Lan, X.L.; Zheng, S.X.; Li, L.P.; Liu, C.Q. Assessment on required separation length between adjacent bridge segments to avoid pounding. *Soil Dyn. Earthq. Eng.* **2019**, *120*, 398–407. [CrossRef]
17. Zhou, L.; Wang, X.; Ye, A. Low cycle fatigue performance investigation on Transverse Steel Dampers for bridges under ground motion sequences using shake-table tests. *Eng. Struct.* **2019**, *196*, 109328. [CrossRef]
18. Saiidi, M.S.; Vosooghi, A.; Nelson, R.B. Shake-table studies of a four-span reinforced concrete bridge. *J. Struct. Eng.* **2013**, *139*, 1352–1361. [CrossRef]
19. Kun, C.; Jiang, L.; Chouw, N. Influence of pounding and skew angle on seismic response of bridges. *Eng. Struct.* **2017**, *148*, 890–906. [CrossRef]
20. Li, B.; Chouw, N. Experimental investigation of inelastic bridge response under spatially varying excitations with pounding. *Eng. Struct.* **2014**, *79*, 106–116. [CrossRef]
21. Li, N.; Xu, W.; Chen, Y.; Yan, W. Experimental research on adjacent pounding effect of midspan curved bridge with longitudinal slope. *Eng. Struct.* **2019**, *196*, 109320. [CrossRef]
22. Yang, Z.; Meng, D.; Chouw, N. Effect of pier height and support flexibility on seismic response of bridges including poundings. *Adv. Struct. Eng.* **2022**, *25*, 1449–1468. [CrossRef]
23. Ding, M.; Xu, W.; Wang, J.; Chen, Y.; Du, X.; Fang, R. Seismic performance of prefabricated concrete columns with grouted sleeve connections, and a deformation-capacity estimation method. *J. Build. Eng.* **2022**, *55*, 104722. [CrossRef]
24. Liu, Y.; Zhou, B.; Cai, J.; Lee, D.S.; Deng, X.; Feng, J. Experimental study on seismic behavior of precast concrete column with grouted sleeve connections considering ratios of longitudinal reinforcement and stirrups. *Bull. Earthq. Eng.* **2018**, *16*, 6077–6104. [CrossRef]
25. Xin, G.; Xu, W.; Wang, J.; Yan, X.; Chen, Y.; Yan, W.; Li, J. Seismic performance of fabricated concrete piers with grouted sleeve joints and bearing-capacity estimation method. *Structures* **2021**, *33*, 169–186. [CrossRef]
26. Ding, Y.; Xu, W.; Chen, Y.; Wang, J.; Yan, W. Experimental research on seismic performance of precast cogging high-strength bolt composite joint and influence of its arrangement location. *Eng. Struct.* **2020**, *225*, 111294. [CrossRef]
27. Liu, H.; Chen, J.; Xu, C.; Du, X. Seismic performance of precast column connected with grouted sleeve connectors. *J. Build. Eng.* **2020**, *31*, 101410. [CrossRef]
28. Lu, Z.; Huang, J.; Dai, S.; Liu, J.; Zhang, M. Experimental study on a precast beam-column joint with double grouted splice sleeves. *Eng. Struct.* **2019**, *199*, 109589. [CrossRef]
29. Xu, T.; Li, Q.; Zhao, R.; Ding, J.; Zhan, Y. On the early-age bond-slip behavior of an eccentric bar embedded in a grouted sleeve. *Eng. Struct.* **2019**, *190*, 160–170. [CrossRef]
30. Wang, S.; Xu, W.; Wang, J.; Xin, G.; Chen, Y.; Zhao, Z.; Bai, Y. Experimental research on anti-seismic reinforcement of fabricated concrete pier connected by grouting sleeve based on CFRP and PET materials. *Eng. Struct.* **2021**, *245*, 112838. [CrossRef]
31. Chen, X.; Guan, Z.; Li, J.; Spencer, B.F., Jr. Shake table tests of tall-pier bridges to evaluate seismic performance. *J. Bridge Eng.* **2018**, *23*, 04018058. [CrossRef]
32. *GB 50010-2010*; Code for Design of Concrete Structures. Architecture & Building Press: Beijing, China, 2015.
33. Shen, B.; Xu, W.; Wang, J.; Chen, Y.; Yan, W.; Huang, J.; Tang, Z. Seismic control of super high-rise structures with double-layer tuned particle damper. *Earthq. Eng. Struct. Dyn.* **2021**, *50*, 791–810. [CrossRef]
34. Zhang, C.; Lu, J.B.; Jia, H.Y.; Lai, Z.C.; Li, X.; Wang, P.G. Influence of near-fault ground motion characteristics on the seismic response of cable-stayed bridges. *Bull. Earthq. Eng.* **2020**, *18*, 6375–6403. [CrossRef]
35. Xin, L.; Li, X.; Zhang, Z.; Zhao, L. Seismic behavior of long-span concrete-filled steel tubular arch bridge subjected to near-fault fling-step motions. *Eng. Struct.* **2019**, *180*, 148–159. [CrossRef]
36. Zhang, X.; Wang, Q.; Ren, Q.; Liu, W.; Ding, W. Finite element analysis of prefabricated concrete box structure system on OpenSees software. In *IOP Conference Series: Earth and Environmental Science*; IOP Publishing: Bristol, UK, 2021; Volume 791, p. 012036. [CrossRef]
37. Yang, Z.; Li, C.; Liu, L.; Yang, H.; Zhong, T. Study on modeling method of reinforced concrete pier based on OpenSees. *J. Phys. Conf. Ser.* **2021**, *18381*, 012034. [CrossRef]
38. Scott, B.D.; Park, R.; Priestley, M. Stress-Strain Behavior of Concrete Confined by Overlapping Hoops at Low and High Strain Rates. *ACI J.* **1982**, *79*, 13–27. [CrossRef]
39. Sarkar, N.; Dasgupta, K. Comparative study of concrete models in OpenSEES for performing nonlinear analysis. In *International Conference on Structural Engineering and Construction Management*; Springer: Cham, Switzerland, 2021; pp. 1135–1143. [CrossRef]
40. Lu, J.Y.; Lin, G. OpenSees Documentation FRP Confined Concrete02. In *OpenSeesPy Documentation*; Oregon State University: Corvallis, OR, USA, 2020; pp. 122–127. Available online: https://www.researchgate.net/publication/340915532_OpenSees_Documentation_FRPConfinedConcrete02 (accessed on 19 July 2022).